

# Journal of Biomedical Optics

[SPIEDigitalLibrary.org/jbo](http://SPIEDigitalLibrary.org/jbo)

## **Lensless multispectral digital in-line holographic microscope**

James P. Ryle  
Susan McDonnell  
John T. Sheridan

# Lensless multispectral digital in-line holographic microscope

James P. Ryle,<sup>a,b,c</sup> Susan McDonnell,<sup>d</sup> and John T. Sheridan<sup>a,b,c</sup>

<sup>a</sup>University College Dublin, Communications and Optoelectronic Research Centre, Belfield, Dublin D4, Ireland

<sup>b</sup>University College Dublin, SFI Strategic Research Cluster in Solar Energy Conversion, Belfield, Dublin D4, Ireland

<sup>c</sup>University College Dublin, School of Electrical, Electronic and Communications Engineering, Belfield, Dublin D4, Ireland

<sup>d</sup>University College Dublin, School of Chemical and Bioprocess Engineering, College of Engineering, Mathematical, and Physical Sciences, Belfield, Dublin D4, Ireland

**Abstract.** An compact multispectral digital in-line holographic microscope (DIHM) is developed that emulates Gabor's original holographic principle. Using sources of varying spatial coherence (laser, LED), holographic images of objects, including optical fiber, latex microspheres, and cancer cells, are successfully captured and numerically processed. Quantitative measurement of cell locations and percentage confluence are estimated, and pseudocolor images are also presented. Phase profiles of weakly scattering cells are obtained from the DIHM and are compared to those produced by a commercially available off-axis digital holographic microscope. © 2011 Society of Photo-Optical Instrumentation Engineers (SPIE). [DOI: 10.1117/1.3659681]

Keywords: digital imaging; holography applications; multispectral imaging; imaging systems; digital processing.

Paper 11290PR received Jun. 8, 2011; revised manuscript received Sep. 21, 2011; accepted for publication Oct. 20, 2011; published online Dec. 16, 2011.

## 1 Introduction

The first lensless holographic imaging microscope system was serendipitously discovered by Gabor in the late 1940s in an attempt to overcome aberrations in the magnetic lenses used in electron microscopy.<sup>1</sup> His concept involves recording an objects diffraction pattern using radiation emitted from a single point source. Nondiffracted light from the same single point source acts as the reference beam, and the scattered light, from the objects placed in-line, interferes with the unscattered reference light beam. This is the original in-line holographic geometry.

It was not until the early 1960s that Leith and Upatnieks would suggest, based on signal processing considerations, the use of an off-axis interferometric geometry.<sup>2-4</sup> This overcame many of the limitations in the Gabor setup, by angularly separating the twin image from the object image. In addition to this, nontransmissive and highly scattering objects could also be holographically imaged with the introduction of the separate reference beam.

The in-line geometry has been applied to electron holography<sup>5,6</sup> as well as microscopy for the study of 3-D trajectories of plankton (copepod nautilplus),<sup>7</sup> imaging microspheres,<sup>8-11</sup> tracking particles in space and time,<sup>12</sup> inspection of deposits on silicon wafers,<sup>13</sup> as well as for the imaging of cancer cells.<sup>10,11,14</sup> The technique has also been employed to image objects using sources of varying wavelengths and degrees of coherence.<sup>10,13,15-18</sup>

Digital holography's (DH) genesis dates back to the late 1960s when Goodman and Lawrence used a Helium-Neon

(HeNe) laser and a Vidicon camera to capture a 256×256 pixel digital hologram.<sup>19</sup> In the mid-1990s, Schnars and Jüptner reported megapixel off-axis DH trumpeting the onset of a new era of DH based whole-field measurement technology.<sup>20</sup>

Implementing a digital in-line holographic microscope (DIHM)<sup>9</sup> involves combining Gabor's lensless in-line geometry and digital holographic techniques (i.e., digital capture, numerical processing and display). In a lensless in-line setup, the weakly scattered light from the sample is the object beam, while unscattered incident light acts as the reference beam. The superposition of these two beams at some distance from the object results in the interference pattern, commonly referred to as the holographic intensity. This is recorded by a light-sensitive optoelectronic detector array, typically a charged-coupled device (CCD) or complementary metal oxide semiconductor (CMOS)-based cameras. This two-dimensional sampled intensity image is numerically processed, and the object wavefront is reconstructed [i.e., a complex image (hologram) having both amplitude and phase information at the location of the object is extracted]. Using multiple computer-based amplitude reconstructions at differing depths (i.e., by simulating the backpropagation of the field through space), a volume or tomographic image surface of imaged features is rendered.<sup>21</sup> As with standard imaging systems, greater lateral and longitudinal resolution is achievable by increasing the systems numerical aperture (NA).<sup>22</sup> However, in the case of digital holographic reconstruction, the resolution depends on the location of the plane examined.<sup>23-25</sup>

In DH systems, the conjugate or twin image is present and acts as a noise signal, obstructing part of the desired reconstructed in-focus object image. Methods have been devised that minimize the effects of the twin image on in-line holographic

Address all correspondence to: John T. Sheridan, University College Dublin, School of Electrical, Electronic and Communications Engineering, Belfield, Dublin D4, Ireland; Tel: 353-1-716-1927; Fax: 353-1-283-0921; E-mail: john.sheridan@ucd.ie.

system performance.<sup>5,26–28</sup> By capturing a number of interference patterns with varying phase shifts of the reference beam, the averaged image intensity or direct current (DC), and twin image terms can be eliminated.<sup>26</sup> A variation of this method exists where the recorded pattern is altered by recording holograms at different planes.<sup>29,30</sup> In the analysis of the lensless system described in this paper, the twin image is considered to be out of focus and thus “smeared out” over the hologram intensity at the camera.<sup>22</sup> Similar to the case of Fraunhofer holography, the effects of the twin image are assumed negligible (see Ref. 6). However, as the hologram is processed and numerically propagated back to the axial planes, the twin image becomes further defocused and the power associated with it spreads over the entire reconstruction window. It is important to note that in the numerical simulation the power associated with the twin image remains constant for each reconstruction plane because the propagation algorithm conserves power. For our purposes we have found that the out-of-focus twin image does not overly compromise the imaging performance of the system.

The minimum resolvable spatial period is dependant on the spacing between the camera pixels (i.e., the sampling points), as governed by the Nyquist sampling theorem.<sup>31</sup> Camera pixels have defined sizes and areas and are evenly spaced (i.e., uniform sampling). Currently available lower pixel widths range from 4.4  $\mu\text{m}$  (in the visible)<sup>32</sup> to 30  $\mu\text{m}$  (mid-IR),<sup>33</sup> while ultraviolet cameras are available with pixel widths of 8  $\mu\text{m}$ .<sup>18</sup> Although the pixel size ultimately limits the spatial resolution, in-line capture techniques make full use of the camera sampling space bandwidth product (SBP).<sup>34</sup> When using such digital optoelectronics, the input wavefield can be magnified using lenses reducing the field of view but potentially increasing the spatial resolution measured using particular digital cameras. High-magnification classical microscopes have limited depths of focus (DOF);<sup>35</sup> however, using a single-captured hologram intensity, it is possible to numerically focus to reconstruct images at multiple depths.<sup>7,22</sup>

Biological samples (i.e., cells) are quasi-transparent weakly scattering objects and typically are stained to aid in conventional incoherent microscopic imaging. If staining is impractical, then phase-contrast methods<sup>36,37</sup> can be employed to make such samples visible. With careful interpretation, DIHM provides access to the complex amplitude of an optical field over a number of axial depths increasing the effective DOF.<sup>7,38</sup> This is convenient as it eliminates the need to manually refocus conventional microscope systems or to mechanically scan using, for example, confocal systems.<sup>39</sup> It also provides access to both the object field amplitude and phase information, and access to such phase information is particularly useful when imaging weakly scattering transparent objects, such as biological cells in solution.

Because of the finite spatial frequency support of the hologram, DH cannot produce full three-dimensional (3-D) images. Because of this, DH whole field imaging has been accurately referred to as a “two-and-a-half-dimensional ( $2\frac{1}{2}$ -D) imaging science”.<sup>24,25</sup> Full 3-D images of thick samples can only be produced using scanning techniques that optically section the object (i.e., collect light from each depth plane with identical NAs). Thus, multiple images are acquired that are focused at different depths through the object, which has the effect of increasing the frequency support of the coherent transfer function (CTF). Confocal microscopy<sup>40</sup> and optical coherence tomography<sup>41</sup> (OCT)

are both examples of 3-D optical sectioning techniques. Using such scanning optical techniques, a full 3-D volume image, with uniform resolution, in  $x$  and  $y$  at each depth throughout, can be obtained.<sup>39</sup>

Industrial-scale bioprocessing (i.e., the growth of cells to produce medicines as by products) is of significant commercial importance. Cells lines such as Chinese Hamster Ovary (CHO),<sup>42</sup> Baby Hamster Kidney (BHK),<sup>43</sup> and mouse myeloma<sup>44</sup> (NS0) are grown in large-scale bioreactors (typically, >1000 l) in the biopharmaceutical (biopharma) industry for the production of various medicines. Examples include Enbrel<sup>®</sup> (Pfizer, until recently Wyeth)<sup>45</sup> used as an anti-arthritis treatment, Herceptin<sup>®</sup> (Roche, until recently Genentech)<sup>46</sup> used in breast cancer treatment, or Epogen<sup>®</sup> (Amgen)<sup>47</sup> used to increase and maintain a high level of red blood cells. Cells are cultured in a growth medium containing nutrients and are classified as either anchorage dependent or independent. Anchorage-independent cells grow in suspension and are constantly agitated and mixed in the bioreactor during the production process. Anchorage-dependent cells grow attached to a substrate, generally plastic. These kind of cells are known as adherent cells and include the MCF-7 (Ref. 48) and MDA-MB-231 (Ref. 49) human cancer cell lines examined later in this paper.

Cell numbers increase exponentially over the duration of the culture period provided environmental conditions are optimal.<sup>50</sup> For exponential growth to occur, the various cell cultures require the provision of (i) Sufficient nutrients and oxygen ( $\text{O}_2$ ) (ii) a constant temperature of  $\sim 37^\circ\text{C}$  and (iii) space to multiply. Should any one of these culture parameters be limited, the cells will not grow at an exponential rate and the resultant productivity will be reduced. If growth conditions continue to deteriorate, then cells will die either by uncontrolled death (i.e., necrosis) or programed cell death (i.e., apoptosis). In large-scale mammalian cell processes, the ability to count the total number of cells and to distinguish between living (viable) and dead (non-viable) cells provides a cell viability estimation. Percentage confluence refers to the density of cells in their growth environment. For adherent cells, 100% confluence means the entire 2-D growth surface is occupied by cells, which will effectively limit the growth of further cells.

Until recently,<sup>51</sup> monitoring cell growth was done off-line and typically involved a skilled technician using a haemocytometer to manually count cells. Using an area marked with a predefined grid pattern etched onto the bottom of the haemocytometer, and knowing *a priori* the volume of the culture sample, an estimate of the average number of cells was made and the cell density determined. Staining the sample with a chemical dye (e.g., Trypan Blue), allowed an estimate of cell viability to be made. Trypan Blue penetrates cells by entering the compromised membrane surrounding dead cells; thus, it only stains nonviable cells. Recently, an automated commercial system, Vi-Cell (Beckman Coulter)<sup>52</sup> was developed to perform off-line cell counts using Trypan Blue assay analysis involving two-dimensional hyperspectral incoherent image analysis.<sup>53</sup> The ability to count cell numbers and estimate cell densities is critical in allowing biopharma production line engineers to monitor growth and to determine the optimum time to transfer cells into larger volume production vessels (i.e., larger bioreactors).

In this paper, a compact lensless DIHM using visible light, based on the lensless microscopic holographic imaging prin-

ciple is described. DIHM experiments involving the use of sources with varying spatial coherence are reported. A single-wavelength helium–neon (HeNe) laser and a multispectral tunable HeNe laser<sup>54</sup> (Research Electro-Optics Inc. Boulder, Colorado) are used as the coherent light sources. One of the attributes of the tunable source is that it produces multiple illuminating wavelengths making coherent multispectral imaging possible. An incoherent tricolor LED (Ref. 55) was used as the incoherent light source. In this case, multispectral imaging is also possible with the advantage that all three separate incoherent sources are compactly located on a single inexpensive device (i.e., the three LEDs are collocated on a single metal holder base, powered separately, and emitting light with different peak wavelengths).

Speckle is a phenomenon associated with coherent sources (i.e., laser illumination) and is a source of noise in imaging systems. A speckle pattern, arising due to diffraction, is generated when light is reflected from rough surface or passes through a random media.<sup>56</sup> Using partially coherent optical sources for illuminations (i.e., passing LED light through a pinhole), speckle effects decreased. However, lower visibility interference fringes are formed resulting in a decrease in the resolution of the imaging system.

We report the capture and processing of a variety of DIHM images in order to test our DIHM performance. These include images of communication-band single-mode optical fibers, 10- $\mu\text{m}$ -diam latex microspheres, as well as adherent MCF-7 and MDA-MB-231 cancer cells. Both amplitude and phase images are extracted from the processed holograms. From the reconstructed images, it is possible to localize areas of interest and, for example, to perform cell counting. In this way, the cell percentage density and percentage confluence can be found. It is also shown to be possible to combine image data obtained for different illumination wavelengths to produce pseudocolor images. Such multiple simultaneous measurement are explored, which might lead to an off-line system capable of assisting in cell viability analyses.

## 2 Theory

Figure 1 shows a schematic of the setups used in this paper for both coherent [Fig. 1(a)] and partially coherent [Fig. 1(b)] illumination. For coherent illumination, the primary lightsource is a laser emitting light at wavelength  $\lambda$ . This is focused onto a pinhole by a microscopic objective lens. The pinhole acts to spatially filter the laser light, removing higher order aberrations and phase front distortions. For partially coherent illumination, the primary lightsource, an LED with peak emission at wavelength  $\lambda$ , is located close to a pinhole. In the case of the LED, the pinhole acts to increase the spatial coherence of the light incident on the object. However, increasing the spatial coherence using smaller pinholes has the drawback that less optical power is transmitted to illuminate the object. Placing the LED close to the pinhole ensures a higher proportion of the LED light is available for imaging because the emitted LED power falls off in proportion to the square of the separation distance.<sup>57</sup>

In both the LED and laser cases, light from the pinhole acts as a secondary source that is used to illuminate the object placed in the DIHM. This point source emits a spherical wavefront. The object is placed at a distance  $z_0$  away from the pinhole, with the

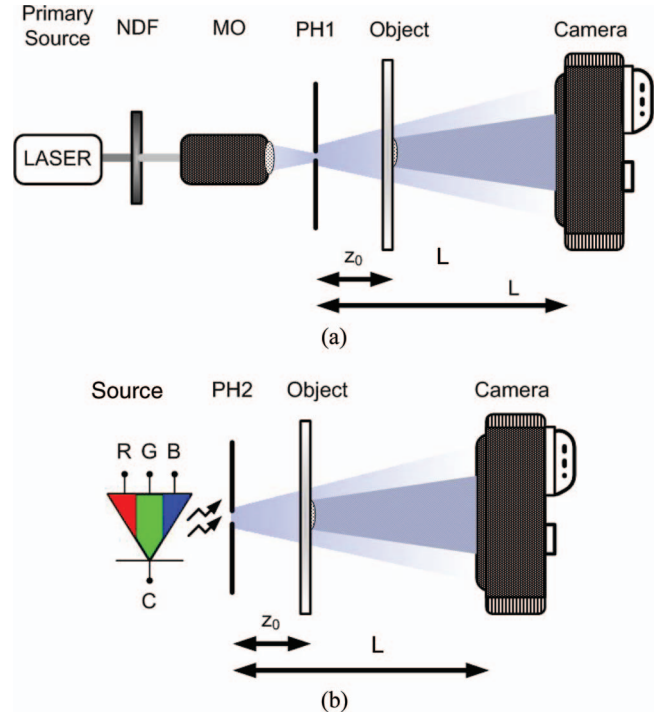


**Fig. 1** Experimental setup for (a) laser illumination where light power from the laser (primary source) is controlled using an NDF before being focused by a 20X microscopic objective (MO) lens onto a 15- $\mu\text{m}$  pinhole (PH1). The second setup (b) the incoherent primary source illuminating a 10- $\mu\text{m}$  pinhole (PH2). The object is illuminated by a spherical wave emitted from the pinhole and captured by a digital camera.

detector array (e.g., CCD or CMOS camera) positioned behind the sample, a distance  $L$  away from the pinhole such that  $L > z_0$  (see Fig. 1). The size of the image formed at the camera plane is dependant on the geometrically magnified diffraction pattern of the spherical wavefront; hence, the system is considered a lensless imaging system<sup>9</sup> with a lateral magnification, based on the geometry, given by  $M = L/z_0$ .

Given a given imaging sensor's sampling pixel width of  $T$ , the minimum resolvable distance is twice this (i.e.,  $T_{\text{samp}} = 2T$ ), while in practice, oversampling (i.e.,  $T_{\text{samp}} \gg 2T$ ) is required to overcome aliasing and noise. Using a collimated beam in a lensless setup would therefore adequately note image particles with diameters comparable to the pixel width. Of course, magnification is introduced by use of spherical wave-producing magnified images, resulting in a minimal resolution capable of imaging particles with comparable diameters to the sensor pixel width.

In the lensless setup, the NA of the system is defined as  $\text{NA} = n \sin(\theta)$ , where  $n$  is the refractive index of the propagating medium and  $\theta$  is the half angle of illumination.<sup>22</sup> Considering the setup geometry in Fig. 2, an expression for the NA is obtained using the limiting factor of the camera chip width,  $W$ , and the propagation distance,  $L$ , from the point source to the camera. Assuming a refractive index of air  $n = 1$  and small angles of illumination (paraxial conditions) such that  $\sin(\theta) \approx \theta$  radians, then

$$\text{NA} \approx \frac{W}{2} \left[ \left( \frac{W}{2} \right)^2 + (L)^2 \right]^{-1/2}. \quad (1)$$



performed as follows:

$$\Gamma(\xi, \eta, z) = \mathfrak{F}^{-1} \{ \mathfrak{F} [H(x, y)](\xi, \eta, z) \times \mathfrak{F} [g(\xi, \eta, z)] \}, \quad (7)$$

where  $\mathfrak{F}(\cdot)$  denotes the Fourier transform.

Equation (7) permits rapid computation using two fast Fourier transform (FFT) and one inverse FFT executions. The reconstructed complex object image  $\Gamma(\xi, \eta, z)$  contains both amplitude,

$$|\Gamma(\xi, \eta, z)| = \sqrt{\text{Re}[\Gamma(\xi, \eta)]^2 + \text{Im}[\Gamma(\xi, \eta)]^2}, \quad (8)$$

and wrapped phase information,

$$\varphi_w(\xi, \eta, z) = \arctan \left\{ \frac{\text{Im}[\Gamma(\xi, \eta)]}{\text{Re}[\Gamma(\xi, \eta)]} \right\}, \quad (9)$$

at the effective image reconstruction depth,<sup>13,16</sup>

$$D_{\text{eff}} = \frac{L}{z_0} (L - z_0). \quad (10)$$

We note that this depth value,  $D_{\text{eff}}$ , is used in all numerical back-propagation calculations in place of the actual physical distance  $L - z_0$  [i.e.,  $z = D_{\text{eff}}$  in Eq. (5)] to correct for the effects of using a point source (i.e., a diverging spherical wave illumination).<sup>61</sup>

As stated, if the object is weakly scattering and highly transmissive (i.e., a phase object causing small intensity variations in transmission compared to the reference wave), then it is possible to obtain the phase information<sup>58</sup> using the in-line geometry. A numerical difficulty in performing continuous phase extraction from digital holograms is the discontinuities due to the modulo  $2\pi$  nature of the arctangent operation appearing in Eq. (9). In order to obtain the continuous phase map,  $\varphi(\xi, \eta)$ , of the true shape, the discontinuous wrapped phase,  $\varphi_w(\xi, \eta)$ , must be unwrapped by adding or subtracting integer numbers of  $2\pi$  to the wrapped phase. Accurate two-dimensional phase unwrapping<sup>62,63</sup> is a nontrivial problem. The exact same algorithm reported by Schofield et al.<sup>63</sup> is used in this paper to perform phase unwrapping calculations. Erroneous phase additions/subtractions can be carried out due to numerical and speckle noise with speckle fields containing phase vortices (singularities),<sup>64</sup> which can greatly complicate unambiguous phase unwrapping.

Following holographic reconstruction, digital processing of the hologram data can be performed to identify and locate objects of interest. For simplicity in this paper, the amplitude and phase of a typical cell is selected from the reconstructed holograms and used as a reference representing the desired object. We refer to this as the reference object. Such a reference object, when cross-correlated with the reconstructed image, yields areas of high correlation, indicating likely object locations. A binary threshold can then be applied to the resulting cross-correlation image with areas above the threshold marked “of interest” and other areas neglected. The choice of threshold value is discussed in Sec. 4.4.

### 3 System and Samples

Schematic diagrams of the experimental systems used are shown in Figs. 1(a) and 1(b). In the first setup, in Fig. 1(a), a monochromatic coherent laser is used as the primary source [i.e., a 20 mW helium–neon (HeNe) laser emitting light at  $\lambda = 632.8$  nm].

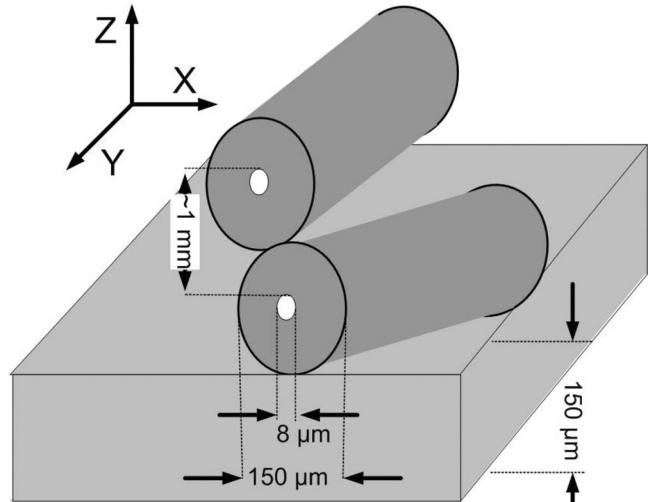


**Fig. 3** Schematic of the two telecommunications optical fibers on a 150- $\mu\text{m}$ -thick glass slide.

For multispectral coherent illumination, a tuneable HeNe laser (Research Electro-Optics Inc.)<sup>54</sup> is used as the primary light source. This can be tuned to emit light at  $\{632.8, 612, 604, 594, \text{ and } 543 \text{ nm}\}$  having maximum optical powers of  $\{4.0, 2.5, 0.5, 0.6, \text{ and } 0.43 \text{ mW}\}$ , respectively. The intensity incident on the sample is first controlled using a neutral density filter (NDF) before being focused by a 20X microscopic objective (MO) lens through a 15- $\mu\text{m}$  spatial filtering pinhole (PH1). The second setup, in Fig. 1(b), involves LED illumination. A tricolor LED<sup>55</sup> is used as the primary source. This consists of three separate square LEDs collocated around the center of a piece of aluminum that acts to dissipate heat during operation. The peak spectral output from each LED was measured, using a spectrometer (BM100), to be at 651, 539, and 474 nm. A 10- $\mu\text{m}$  pinhole (PH2) positioned  $\sim 1$  mm from the secondary source acts to increase the spatial coherence of the light. The emitted light from the pinhole secondary source is then incident and scattered by the object. The resulting intensity patterns are then captured using a monochromatic digital camera in each system [Imperx 1M48 (1000  $\times$  1000 pixels); pixel pitch: 7.4  $\mu\text{m}$ ].

Numerical reconstruction was performed using a laptop with an Intel P8400 Core Duo processor with clock speeds of 2.26 GHz per processor and with 3 GB of RAM. The MATLAB 7.4.0 (R2007a) (Mathworks Inc.) programming environment was used to implement the Kirchhoff–Helmholtz reconstruction algorithm [i.e., Eq. (5)] and for all other data processing operations. Thus, the DIHM was implemented using commonly available relatively inexpensive optical components and optoelectronics.

Several objects were imaged using the proposed lensless DIHM, including optical fibers, latex microspheres, and cancer cells. The optical fibers and latex microspheres were used because they provide a convenient means of testing and calibrating the DIHM system. In the case of the optical fibers, two lengths of single-mode 1330-nm communication optical fiber (SM 1340/P2123-R) were positioned as shown in Fig. 3. They were held rigidly in place, using adhesive (Norland optical adhesive 61), on a 150- $\mu\text{m}$ -thick glass slide.

In the case of the latex beads, 1-mm-thick glass slides (Hirschmann Laboratories, ISO 8037/1) provided a substrate for a number of randomly positioned 10- $\mu\text{m}$ -diam latex microspheres (Polyscience Inc., diameter: 9.606  $\mu\text{m}$ , standard deviation: 0.763  $\mu\text{m}$ ) in air. Holographically imaging such objects demonstrates the axial resolving power of the DIHM presented. The availability of such 3-D phase calibration samples are critical to test the lateral and axial imaging abilities of the proposed lensless DIHM.

Cancer cells were also imaged. Human breast cancer cell lines, MCF-7,<sup>65</sup> and MDA-MB-231,<sup>66</sup> were grown in Dulbecco's Modified Eagle's Medium (DMEM) supplemented with 10% foetal calf serum. The cells were cultured in T25 flasks at a temperature of 37°C, with a 5% CO<sub>2</sub> atmosphere. Between  $1 \times 10^4$  and  $5 \times 10^4$  of the cells were placed into each well of a Lab-Tek II 4-well sterile-chambered glass slide. In large-scale bioprocess engineering, cell subculturing is continued up into larger tanks and bioreactors (capable of holding up to 12,500 l) for bulk production. In our case, once the cells had adhered to the glass slide, they were chemically fixed in 100% methanol for 10 min and the raised chamber walls surrounding each separate well were removed. This yielded a total of four wells, two wells (or volumes) for each cell line.

To aid in the imaging of the cell lines using a conventional compound microscope, one well of each of the quasi-transparent weakly scattering samples were typically stained using 0.25% Crystal Violet. Crystal Violet stains the DNA/protein in the nuclei a deep purple color and the cell walls a paler purple. This should not be confused with Trypan Blue staining, which only stains nonviable cells and is used to estimate off-line cell viability. In the DIHM, Crystal Violet was found to be unnecessary to produce useful images.

## 4 Experimental Results

We now present a series of experimental results produced during the calibration and application of the lensless DIHM systems described in Sec. 3. These include the following:

1. The LED spectral output was examined to find the emitted peak wavelength. The emitted optical power was also measured.
2. The performance of the DIHM system was then tested by imaging the optical fibers illuminated using laser light.
3. Cells were holographically imaged using first laser and then LED illumination, with percentage confluence of the samples being estimated.
4. Using single-wavelength laser illumination and applying the scale and rotation invariant filterbank with appropriate thresholding, cell counts were obtained.
5. Multispectral imaging was then performed on cells and latex microspheres using laser and LED light. A comparison to a commercially available white-light bright-field microscope is presented.
6. Finally, a qualitative comparison between the performance of the DIHM presented here and a commercially available off-axis digital holographic microscope (DHM) is presented.

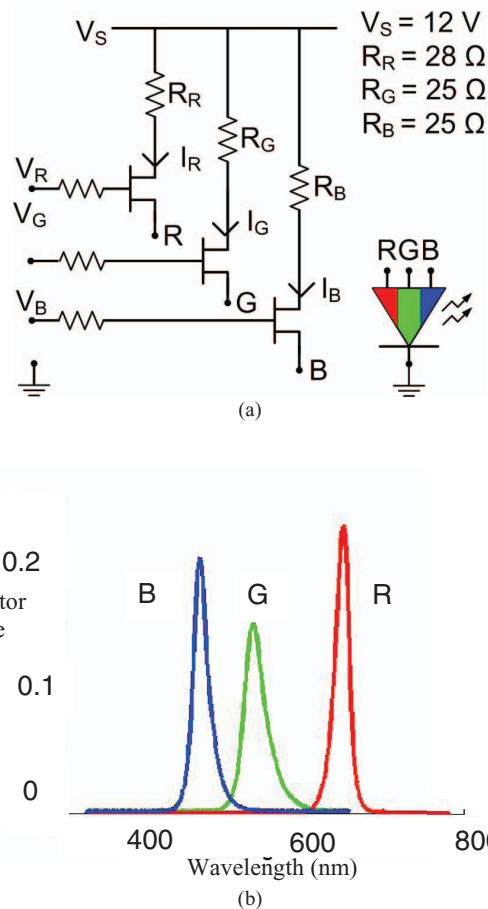


**Fig. 4** (a) An example of the driver circuitry used in controlling illumination RGB LEDs, and (b) measured LED spectral response for  $I_R = I_G = I_B \approx 350$  mA.

### 4.1 Testing

In order to select one particular color output from the tri-colour LED light source, the circuits shown in Fig. 4(a), were designed and built to deliver currents of 350 mA to each of the comounted separate LED sources. Using a supply voltage of 12 V with a 28- $\Omega$  resistor for the red channel and 25- $\Omega$  resistors for the green and blue channels, currents of 350 mA were delivered to each source. A TIP 112 Darlington pair transistor<sup>67</sup> was used as an electronic switch capable of passing high current. Current flow was controlled directly from three pins connected to the computer serial port output connected via 10-k $\Omega$  resistor attached to the base of each transistor.

The spectrum of the LEDs was obtained using a highly resolved, stepper-motor-controlled (KE-10 controller) scanning grating monochromator (BM100) with a grating of 300 lines/nm and a 1-m focal length lens. An EG & G photodiode (UV-444B PN) was used to measure the detected light, and the resulting signal was sampled using a Keithley 6514 system electrometer. The spectral response of each individual LED source, operating with currents of 350 mA, was recorded. Figure 4(b) shows the spectral response obtained using the spectrometer with each spectrum appropriately labeled R for red (651 nm), G for green (539 nm) and B for blue (474 nm). A calibrated Newport power meter (model 2931-C) with a detector head (918D-UV-OD3)

**Table 1** Multispectral LED spectral response and power measurement.

	Red	Green	Blue
Measured Central/peak Wavelength (nm)	651	539	474
Measured 1/2 width peak (nm)	19	31	23
Typical Diode Voltage (V)	2.2–2.8	3.2–3.8	3.2–3.8
Designed Diode Current (mA)	~350	~350	~350
Measured Optical power (mW)	2.071	1.42	2.225

was used to detect the optical power emitted from each LED under the same operating conditions. The measured total output powers from each channel were 2.07 mW (red), 1.44 mW (green), and 2.225 mW (blue) at a distance of 2 cm from the source. Table 1 shows the peak wavelength, half power, and rated breakdown voltage value as well as the operating current used for each spectral channel during the measurement.

#### 4.2 Fiber Depth

Figure 3 is a schematic showing the orientation of two lengths of single-mode 1330-nm communication optical fiber (SM 1340/P2123-R) axially separated on top of a 150- $\mu\text{m}$ -thick glass slide. Holograms were captured with  $\lambda = 632.8$  nm and using a DIHM system with the geometrical parameters of  $L = 50$  mm, with the object located first at  $z_1 = 8.9$  mm and then at  $z_2 = 10$  mm. The resulting magnifications at  $z_1$  and  $z_2$  are  $M_1 = 5.6$  and  $M_2 = 5$ . For our camera,  $W = 7.4$  mm and using Eq. (1), the numerical aperture of the DIHM is  $\text{NA} = 0.074$ . Thus, the predicted lateral and longitudinal resolution of the DIHM are  $\delta x = 4.29$   $\mu\text{m}$  and  $\delta z = 58$   $\mu\text{m}$  [see Eq. (2)].

Before inserting the glass slide containing the optical fibers into the system, the baseline reference illumination  $I_0(x, y, 0)$  was captured by the camera [see Fig. 5(a)]. The resulting intensity hologram [see Eq. (3)] captured by the camera is presented in Fig. 5(b), and the normalized contrast hologram [see Eq. (4)] is shown in Fig. 5(c). The reconstructed bright-field intensity and phase images corresponding to Fig. 5(b) at  $z_1 = 8.9$  mm are given in Figs. 5(d) and 5(g). A noticeable constant background brightness level associated with the DC term is present. The equivalent reconstructed dark-field intensity and phase images at  $z_1 = 8.9$  mm, extracted from the normalized contrast hologram in Fig. 5(c), are presented in Figs. 5(e) and 5(h). The background DC term has been suppressed in Fig. 5(e) compared to 5(d). The thin central single-mode fiber core are visible in both the bright- and dark-field images. The reconstructed dark-field intensity and phase images at  $z_2 = 10$  mm are presented in Figs. 5(f) and 5(i), respectively. These images show the thin central single-mode fiber core occupying approximately 1–2 pixels in width on the image. The two fibers are clearly distinguishable from one another as they are spaced  $\sim 1$  mm apart, a distance that we note is much greater than the minimum axial resolvable distance between two points (i.e.,  $\delta z = 58$   $\mu\text{m}$ ).

The fibers cross in the bottom-left quadrant of the reconstructed images. The top fiber obstructs the view of the bottom fiber, and they are indistinguishable from one another in this area. As noted, digital holography is not a whole-field imaging technique (i.e., not a true 3-D imaging science).<sup>24,25</sup> However, our experimental results do demonstrate the DIHM's ability to perform tomographic whole-field microscopic imaging over a 1-mm object volume depth and with significant lateral resolution.

#### 4.3 Cells: Percentage Confluence and Thresholding

The setup shown in Fig. 1(a) was used to capture the reference illumination intensity as well as a hologram of MDA-MB-231 human cancer cells cultured and prepared as described in Sec. 3. The hologram presented here was captured using coherent laser light ( $\lambda = 632.8$  nm). Setup parameters of  $L = 85$  mm and  $z_0 = 17$  mm give a magnification of  $M = 5$  and a system  $\text{NA} = 0.0435$ . The lateral resolution of the DIHM is therefore predicted to be  $\delta x = 7.25$   $\mu\text{m}$ , which should be sufficient spatial resolution to identify individual MDA-MB-234 cells that have widths of  $\sim 25$   $\mu\text{m}$ .<sup>66</sup> We note that, for ease of processing, the results presented here involve smaller  $512 \times 512$  pixel images ( $0.75 \times 0.75$  mm) extracted from the central region of the original  $1000 \times 1000$  pixel hologram ( $7.4 \times 7.4$  mm).

The normalized contrast hologram was numerically generated using Eq. (4). The resulting contrast hologram is shown in Fig. 6(a), whereas the corresponding intensity reconstruction is shown in Fig. 6(b). The cells are clearly visible in the intensity reconstruction with wrapped phase discontinuities noticeable close to the edges of the cells in the phase image [Fig. 6(c)]. We note that phase discontinuities exist near the edges of the cells and indicate that the phase delay changes exceed  $2\pi$  rad. Continuous phase variations in the range 0 to  $\sim 4\pi$  rad are observed. This corresponds to height variations up to  $\sim 975$  nm, assuming for numerical simplicity a cell refractive index close to that of water (i.e.,  $n_c \approx 1.3$ ).

Figure 7 illustrates a cross section of a highly idealized cell of height  $d$  on a glass slide. The phase-delay difference is caused by the change of refractive index as light passes through air  $n_{\text{air}} = 1$  into the cell  $n_c = 1.3$ . The height profile of the cell is extracted as a function of the refractive indices (cell, air) and the measured phase.

In order to estimate the percentage confluence or cell-content percentage, the individual cells must be identified. To achieve this, a typical representation of a cell-intensity image was first selected from the reconstructed intensity image to act as a reference cell. The reference cell was then cross-correlated with the original intensity image to identify structure/shapes in the image having high similarity to the reference cell. From this, a binary “decision image”, presented in Fig. 6(d), was created by thresholding the correlation image. A crosssection of the normalized autocorrelation of one such typical reference cell is shown in Fig. 8(a). The cross-sectional width of the reference cell corresponds well to a threshold value of 50%. This threshold value is used to classify areas of interest throughout this paper and was chosen because it is sufficiently large not to return many false-positive identifications for the typical baseline background correlated data, nor is it so large as to severely underestimate the percentage confluence by not

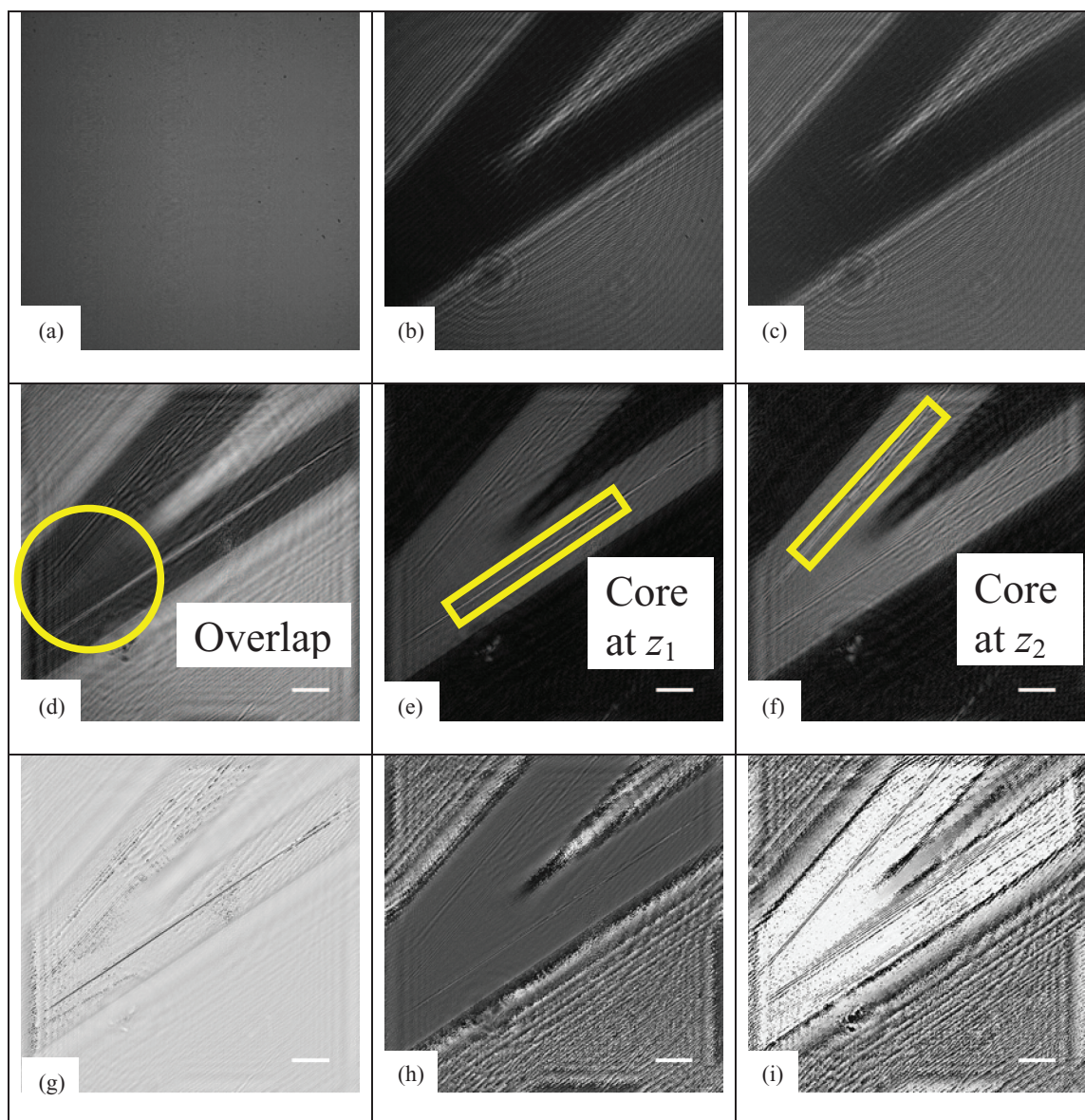


**Fig. 5** Two telecommunication unclad optical fibers axially displaced: (a) Reference illumination intensity, (b) intensity hologram, (c) normalized contrast hologram, bright field (d) intensity and overlaid indicator, and (g) phase reconstruction for  $z_1 = 8.9$  mm with the corresponding dark-field intensity and phase reconstructions shown in (e) and (h) with fiber cores indicated. The dark-field intensity and phase reconstructions for  $z_2 = 10$  mm are shown in (f) and (i). A scale bar of  $75 \mu\text{m}$  is shown in each reconstructed image.

identifying areas of interest (i.e., areas known to contain cells). An illustrative cross-sectional example illustrating the decision process is shown in Fig. 8(b). Regions in the cross-correlation results that have values above the 50% threshold are considered to contain cells. The measured width of the reference cell used in this result is displayed and highlighted using the vertical dashed lines in Fig. 8(a). Applying a lower threshold value of 40% in Fig. 8(b) returns an overestimation in cell identification. Similarly applying a higher threshold value of 60% returns an underestimation.

Thresholding issues also arise in relation to the use of the scaled and rotated versions of the reference cell. These are examined in Sec. 4.4. White areas in Fig. 6(d) represent regions with correlation values above the threshold value and therefore areas within which cells are likely to be present. Black repre-

sents dissimilar areas having a lower probability of containing cell-like shapes. An example of a resulting binary decision image is shown in Fig. 6(d). On the basis of this result, found using the hologram captured with the laser-based DIHM, we have calculated the inspected area to have a 9.03% confluence. This suggests there is sufficient space for adherent cells to grow further. It should be noted that the cell cultures used in this paper were prepared for off-line analysis (postprocessing) and were chemically fixed to the glass slide. For this reason, the percentage confluence result represents a snapshot of the entire batch at the specific time the cells were sampled.

A similar approach was adopted to image the MCF-7 human cancer cells using the LED as the primary source. The setup used was that illustrated in Fig. 1(b). For the results presented in Fig. 9, the red LED channel was selected emitting a peak

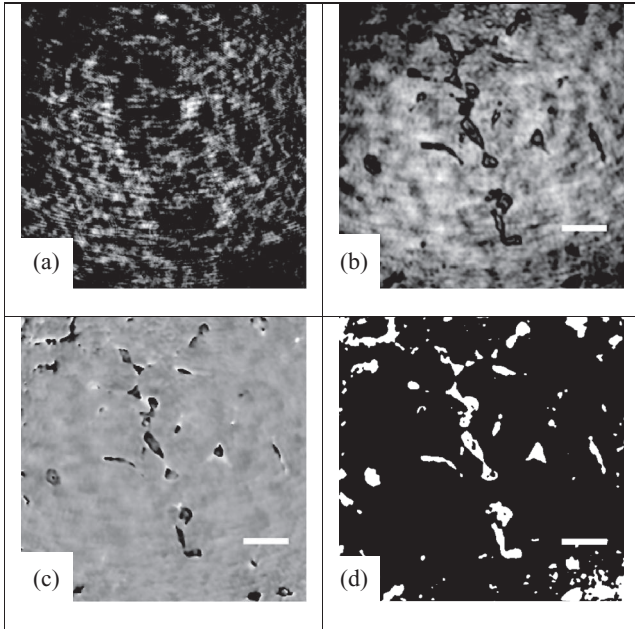


**Fig. 6** MDA-MB-231 mammalian cancer cells: (a) Hologram (b) intensity reconstruction (c) wrapped phase and (d) binary decision map for a 9.01% confluence. A 120- $\mu\text{m}$  scale bar is given in (b–d).

wavelength of 651 nm. Setup parameters of  $L = 30$  mm and  $z_0 = 4.6$  mm give a magnification of  $M = 6.5$  and a system NA = 0.12. The lateral resolution of the DIHM is then  $\delta x = 2.5 \mu\text{m}$ , providing sufficient spatial resolution to image MCF-7 cells, which we recall have widths of  $\sim 25 \mu\text{m}$ .<sup>65</sup>

Unlike the previous result, the  $1000 \times 1000$  pixel contrast hologram was zero padded at the edges (top, bottom, and either side of the image) to produce a hologram with  $1024 \times 1024$  elements [see Fig. 9(a)]. This optimizes the computation time taken by allowing the use of the FFT algorithm in the reconstruction process, as described in Sec. 2. The resulting reconstruction intensity and phase are shown in Figs. 9(b) and 9(c), respectively. A number of MCF-7 cells are visible having the characteristic round/oval shape,<sup>65</sup> indicated by the typical representative cell in Fig. 9(b). Digital image processing was performed on the intensity image to remove vertical and horizontal residual lines that appear due to the numerical zero-padding process. These artifacts remain visible in the phase image because the filter was designed to only remove such artifacts from the intensity image.

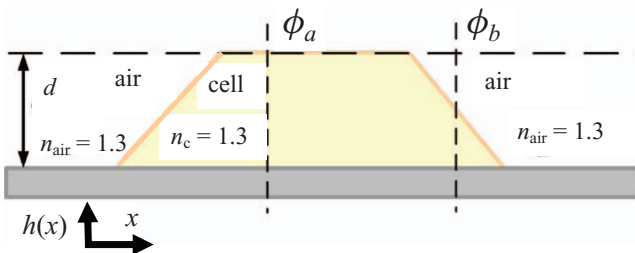


**Fig. 7** Illustration of a cell on a glass substrate showing the position-dependent height profile and phase-delay relationship. Dashed lines indicate the phase delay through the cell,  $\phi_a = 2\pi n_c d / \lambda$ , and through air and the cell  $\phi_b = (2\pi/\lambda)\{n_c h(x) + n_{\text{air}}[d - h(x)]\}$ .

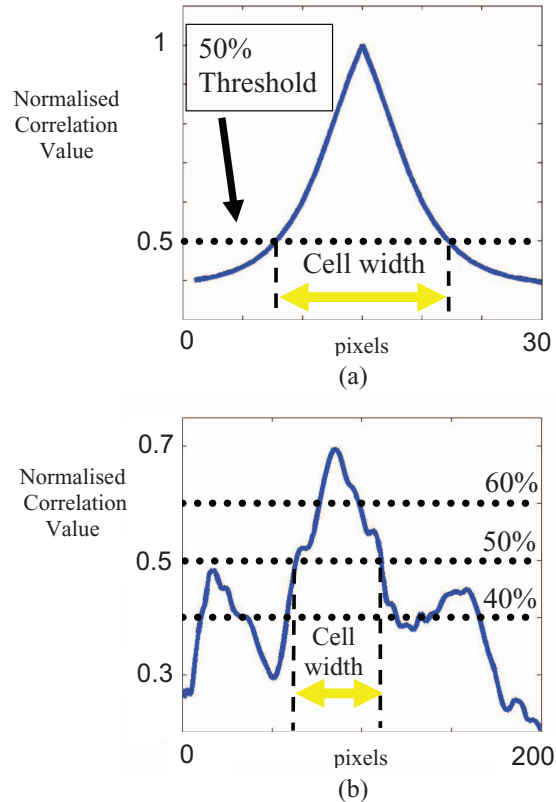


**Fig. 8** (a) Autocorrelation of a typical cell with the threshold value of 50% correctly showing the cell width, while (b) is a cross-section of the cross-correlation of a typical cell and the experimental data. Threshold values of 40, 50 and 60% are shown with 40% overestimating cell location and 60% underestimating cell location. The threshold value of 50% accurately detects the cell width.

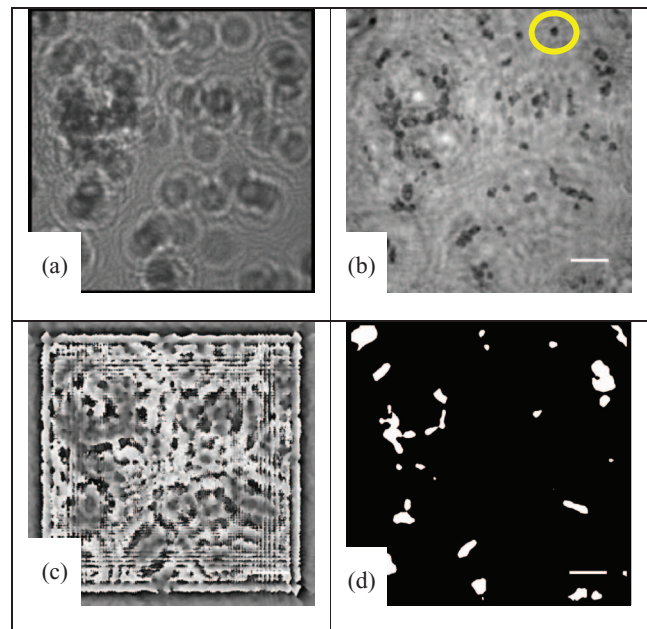


**Fig. 9** MCF-7 mammalian cancer cells illuminated using LED light (651 nm): (a) Hologram, (b) intensity reconstruction with a characteristic cell circled, (c) wrapped phase, and (d) binary decision map for a 4.91% confluence. A 150- $\mu\text{m}$  scale bar is given in (b–d).

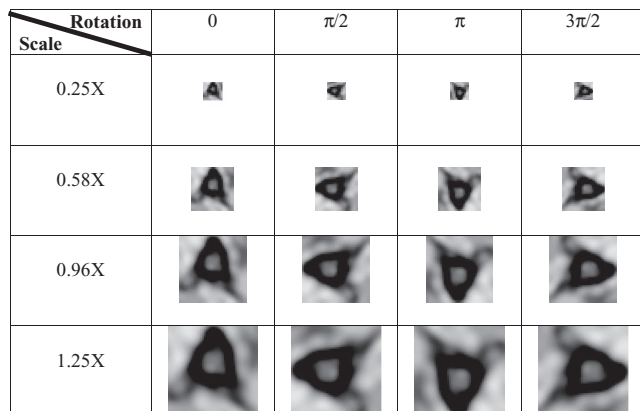


**Fig. 10** Scale and rotation filter bank showing a scaled and rotated representation of a cell used to detect cells.

The phase image produced when using LED illumination [see in Fig. 9(c)], do not result in images as sharp as those obtained using the laser [see Fig. 6(c)]. One of the reasons for this is the limited spatial coherence of the light emitted from the secondary source (pinhole). A pinhole with a diameter of  $10 \mu\text{m} \approx 15\lambda$  was used. However, as noted LEDs are less spatially coherent and have a broader spectral output than lasers. Another factor decreasing visibility is the lower light intensity used to illuminate the object. The total optical power emitted by the red LED before going through the pinhole was measured to be 2.07 mW (see Table 1). This total optical output power from the red LED is only  $\sim 10\%$  of the HeNe laser output power. Furthermore, although most of the laser light is transmitted by the filtering pinhole, only a small fraction of the total red LED light was transmitted by the pinhole, which acts as the secondary source.

Using the same techniques described earlier in this section, the percentage confluence was calculated for LED illumination. Typical cell data were selected from the reconstructed intensity image as a reference image. The reference cell was then cross-correlated with the original intensity image to identify shapes in the image having areas of high similarity to the reference cell. A binary decision image was created by thresholding the correlation image using the correlation value of 50%. Once again in this decision image, white areas represent areas of interest and black areas represented areas below the threshold value. The resulting binary image is shown in Fig. 9(d). From the hologram captured using the laser-based DIHM, we have calculated this area to have 4.91% confluence. As in the MDA-MB-231 result presented in Fig. 6, there appears to be sufficient space for MCF-7 adherent cells to continue to multiply. In the sample examined, they are chemically fixed to the glass slide for off-line analysis. The second confluence result (4.91%) [see Fig. 9(d)] is lower than the first result (9.03%) [see Fig. 6(d)]. From a visual inspection, Fig. 9 does indeed contain fewer cells than Fig. 6.

DIHM measurement of percentage confluence, which indicates the area occupied by cells, has been discussed. Using a correlation-based method, percentage confluence was calculated for two samples, MDA-MB-213 and MCF-7 using both spatially coherent laser illumination (632.8 nm) and spatially incoherent LED (651 nm) illumination. Percentage confluence

was estimated by correlating a typical representative cell over the entire image. A binary decision image was formed by selecting a threshold value. This threshold value was applied over the whole image and as shown was chosen not to produce excessive false results. However, a small portion of the cell area (as shown in Fig. 8) falls below (outside) the threshold cutoff value, thus producing a small underestimate of the percentage confluence. A nonuniform or adaptive thresholding technique<sup>21</sup> could be applied to minimize the error in selecting areas that contain cells, and such techniques can be readily implemented numerically. In this paper, our aim is to provide automated estimating of the percentage confluence values. We must emphasize, that our approach involves minimal data processing.

#### 4.4 Cells: Scale and Rotation Analysis

For industrial biopharma production, the number of cells, or cell density, can be a critically important factor in predicting the conditions for cell growth (see Sec. 1) and, thus, in deciding the optimum time to harvest the cell cultures. Cellular bodies have different sizes during the growth process because the nucleus and cellular contents must be duplicated before the cell divides. In addition to this, the cells may adhere with different orientations onto the glass slide during off-line inspection. In an attempt to recognize and count cells of different sizes having different orientations, a filterbank is built up from scaled and rotated versions of a representative cell image.

Figure 10 shows a magnified image of a typical representation (reference cell) obtained by selecting a  $68 \times 68$  pixel area from a  $600 \times 600$  pixel intensity reconstruction [specifically from the data presented later in Fig. 12(a)]. Figure 10 consists of scaled versions of the same cell at 0.25 ( $24 \times 24$  pixels), 0.58 ( $40 \times 40$  pixels), 0.96 ( $63 \times 63$  pixels), and 1.25 ( $85 \times 85$  pixels) times the original reference cell size. This range of cell sizes covers the typical range observed in the case of an image magnification of  $M = 5$  and includes single cell size to that of a single cell in the process of duplicating. All these scaled versions of the reference cell are angularly rotated counterclockwise by  $0, \pi/2, \pi,$  and  $3\pi/2$  in order to represent various rotated versions of the cells.

Increased detection accuracy can be obtained using a filter bank with a larger number of elements (i.e., of a typical cell versions more closely spaced in size and having smaller rotational differences). However, increasing the number of elements in the filter bank necessitates additional processing. The best result involves the optimal choice of a minimum number of appropriately spaced and rotated images. To test the scale and rotation choices used to generate the filter bank employed in this paper, a comparison of the correlation values between the reference cells (at different scales and rotations) was made. First the 0.96X-scale reference cell at a  $\pi/2$  rotation was cross-correlated with itself yielding its autocorrelation (see Fig. 11). This autocorrelation is used as a basis of comparison to subsequent cross-correlations. To test the rotation values used, a different reference cell in the filter bank was chosen. The cell had the same 0.96X scale but was rotated by an angle of  $\pi$ . This was then cross-correlated with the cell at the 0.96X scale and  $\pi/2$  rotation (as shown in Fig. 11). A maximum correlation value of 0.6135, normalized to the basis cell autocorrelation, was obtained. This correlation value is above the 50% threshold and

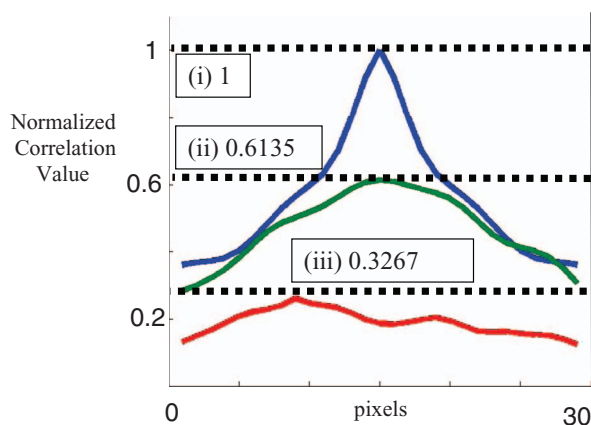


**Fig. 11** Results obtained by cross-correlations scaled and rotated reference images: (i) 0.96X and 0.96X at  $\pi/2$  rotation (autocorrelation), (ii)  $\pi$  and  $\pi/2$  at 0.96X scale, and (iii) 0.96X and 0.58X at  $\pi/2$  rotation. (ii) Has a correlation value of 0.61, suggesting adequate spacing in rotations to allow us to determine cells. However, the 0.32 value of the correlations peak for different scale (0.96X and 0.58X) suggest the filter bank would benefit by having more closely spaced scale in order to reduce the possibility of not recognizing some cells sizes.

suggests cells within the range of rotations would be detected. A similar approach was adopted to test the scale spacing. In this case, the corresponding reference cell at the same  $\pi/2$  rotation as the first cell, but scaled by 0.58X, was cross-correlated with the 0.96X cell. A resulting cross-correlation value, normalized to the autocorrelation, of 0.354 was calculated. This is below the 50% threshold and suggests cells that have sizes between these two scale values may not always be detected using the filter bank presented here. As noted, increasing the number of scaled reference cells should increase the accuracy of cell detection and there will be an associated increase in processing time.

Figure 12 shows the reconstructed intensity, Fig. 12(a) from the same holographic data as presented in Fig. 6. In this case,  $600 \times 600$  pixels ( $0.88 \times 0.88 \text{ mm}^2$ ) are used compared to  $512 \times 512$  in Fig. 6. Although in Fig. 6 it was demonstrated that clear high-contrast DIHM images could be produced using our DIHM, our aim here is to illustrate that the application of our cell-location procedure can be used to produce accurate results over a large field of view. A binary decision image showing cell locations in white is presented in Fig. 12(b). This digital

transmittance mask is combined with the reconstructed intensity image [Fig. 12(a)]. Locations where cells are identified as being likely to exist are highlighted in the reconstructed intensity in Fig. 12(c). The filter bank described here could be used to very rapidly ( $\sim 5$  s using a PC) locate a total of 52 cellular bodies in an area of  $0.789 \text{ mm}^2$ . Despite the limitations of our look-up table approach, the results provide a very good estimation of the number of cells present in the sample. The areas where erroneous cell detection occurred are highlighted in Fig. 12(c). The single square represents an example of an area where a cell is in fact located, but was not detected using the method described here (a false negative). The two circles represent two examples of areas where, on visual inspection, no cells exist, but the algorithm has incorrectly detected two cells (false positives). The total number of cells detected using this method is 52 while 51 areas representing cells were visually identified. This corresponds to 2% false-negative and 4% false-positive automatic cell location identification rates.

The intensity hologram data used to obtain a cell count are the same data used earlier to calculate the 9.01% confluence (see Fig. 6). The growth area present in Fig. 12 is  $0.789 \text{ mm}^2$ . In this field of view, 52 cellular bodies were detected. Cell numbers double during a growth cycle. Because 52 cells result in a 9.01% confluence, then 416 cells occupying 72.08% of the adherent growth area will be present after two further growth cycles. Insufficient space is then available for a further cycle of cell multiplication for the cells adhering to the 2-D glass slide surface. Programed cell death would then occur with a decreased yield of viable MDA-MB-231 cells. Using this off-line measurement technique, an estimate for the optimal time to obtain the optimum yield can be obtained.

Our use of a simple scale and rotation filter, in combination with DIHM, to rapidly identify cells clearly demonstrates the capability to automate cell culture analysis to count cells. In this way, cell density can be rapidly estimated from a single intensity hologram obtained using an inexpensive optical system.

#### 4.5 Multispectral Digital In-Line Holographic Microscope Imaging

The significance of percentage confluence for cell-culture bio-process analysis has been discussed, and the possibility of automatic cell identification and counting has been demonstrated.

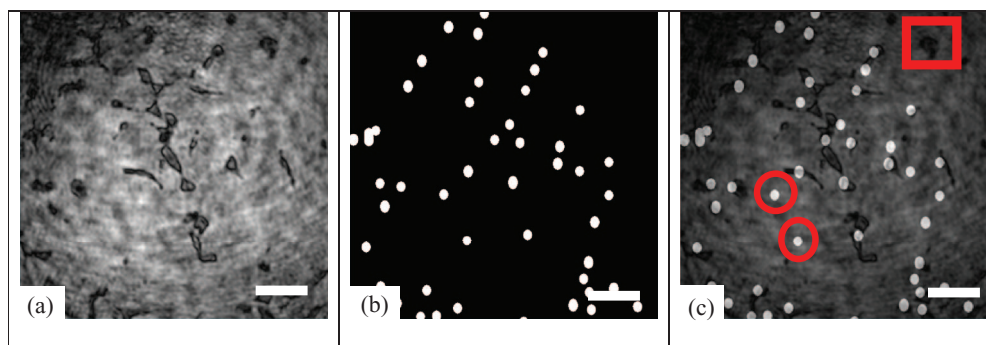


**Fig. 12** (a) MD-MBA-231 reconstructed intensity image and (b) binary image showing cell locations, while (c) shows transmittance mask of (b) superimposed on (a) highlighting detected central locations of cells and actual cell locations. Identification errors are highlighted by overlaid shapes while a  $115\text{-}\mu\text{m}$  scale bar is shown in each result.

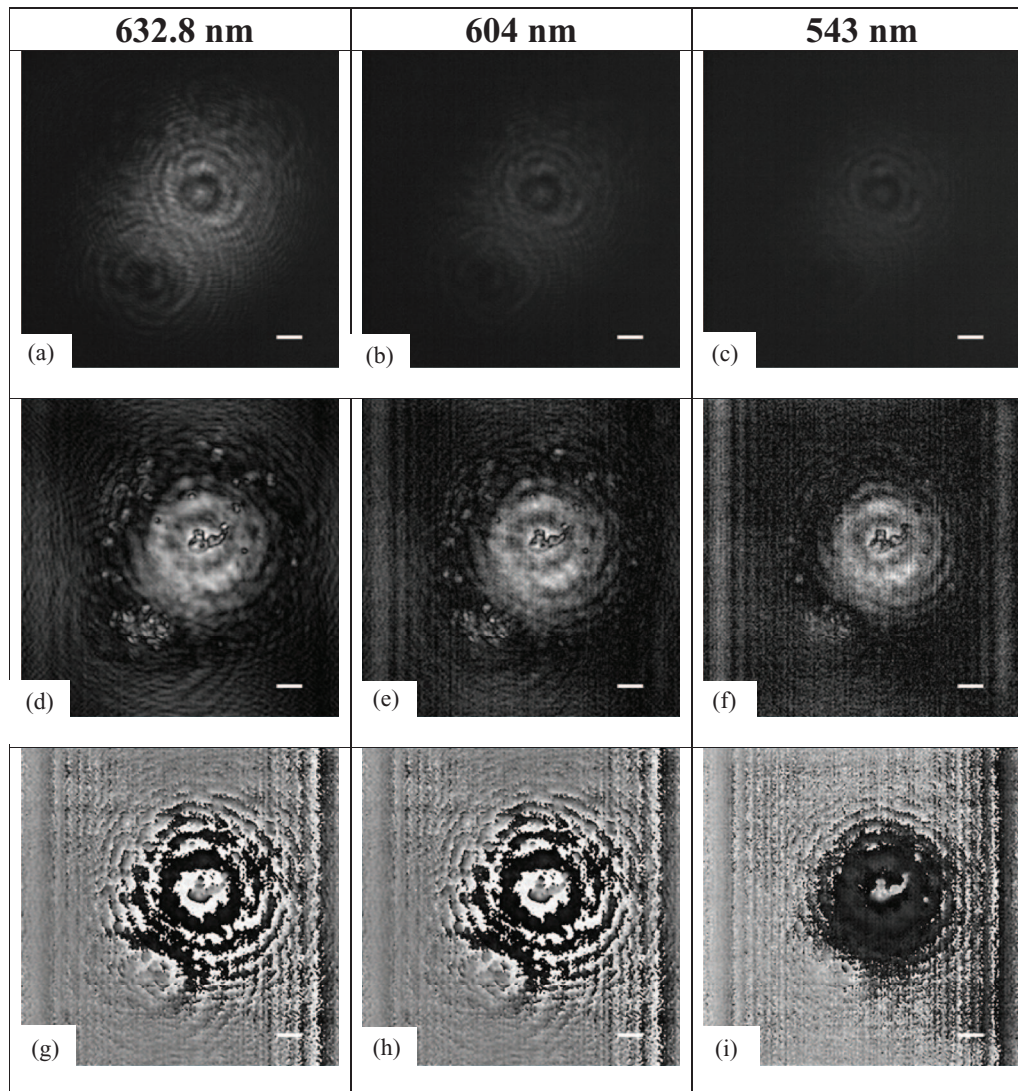


**Fig. 13** Multiple images of the same region of a single MCF-7 human cancer cell using three different illuminating wavelengths, 632.8, 604, and 543 nm. The corresponding holograms, intensity reconstructions, as well as phase images are presented in (a), (d), and (g) for 632.8 nm, while (b), (e), and (h) show results for 604-nm illumination and (c), (f), and (i) show results obtained for 543-nm laser illumination, respectively. Experimental parameters were  $z_0 = 12$  mm,  $L = 80$  mm, magnification = 6.67 and NA = 0.049.

From the total number of cells produced, a mix of viable and nonviable cells as well as necrotic bodies will be present in any sample taken, which may give rise to false positives generating misleading information. An important analysis tool used in the production of biopharmaceuticals is the Trypan Blue assay. Compromised cell membranes allow entry of Trypan Blue into nonviable cells resulting in these having a blueish color while viable cells are not affected. The ability to perform off-line process control spectral analysis in order to locate cells stained blue (i.e., to perform the Trypan Blue assay) might be possible using the DIHM described in this paper. However, before this can be demonstrated, a number of factors must be considered. The Trypan Blue staining dye will absorb wavelengths in the green and blue, complicating phase reconstructions at these wavelengths. Enhanced functionality could be achieved having access to multiple wavelengths especially at wavelengths where color information is key in selecting objects of interest (i.e., such as the Trypan Blue assay).

Recording holograms at different wavelengths using a monochromatic camera requires multiple sequential frame captures. The manually tunable HeNe laser results presented were obtained using illuminating wavelengths of {632.8, 604, and 543 nm}, which have rated optical power outputs from the laser of {4, 0.5, and 0.3 mW} respectively. Three reference illuminations were sequentially applied to a sample slide containing MCF-7 cells held in place in the DIHM with  $L = 80$  mm and  $z_0 = 12$  mm. The resulting magnification is  $M = 6.67$  for a system with NA = 0.0462 (based on system geometry), having lateral resolutions of  $\delta x = \{6.85, 6.53, \text{ and } 5.87 \mu\text{m}\}$ , respectively. These values are all sufficient to image the  $\sim 25\text{-}\mu\text{m}$ -diam MCF-7 cells.<sup>65</sup>

Three resulting normalized contrast holograms are presented in Figs. 13(a)–13(c), respectively. Each of these figures contains information about the same object, but they are not exact replicas of one another due to both (i) the variations in optical power available and (ii) the different wavelengths used. Intensity

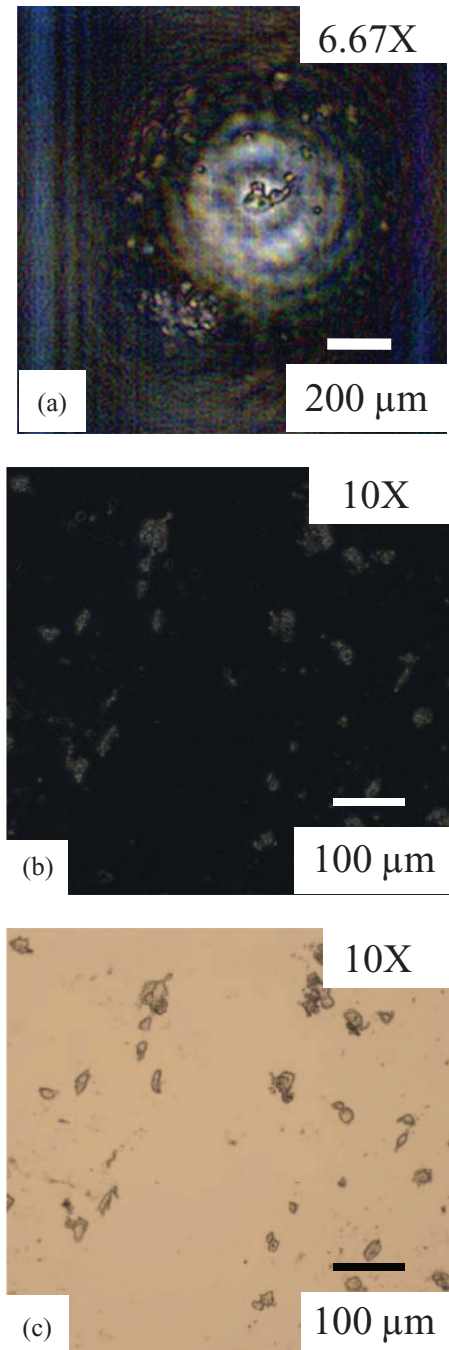


**Fig. 14** (a) Combining the images in Figs. 13(d)–13(f) generated a multispectral dark-field image of MCF-7 cancer cells is generated. Experimental parameters used were  $z_0 = 12$  mm,  $L = 80$  mm, magnification = 6.67, and  $NA = 0.049$ . No correction for wavelength scaling was performed on this image, for comparative purposes, (b) dark- and (c) bright-field images of MDA-MB-231 cells from a commercial microscope are shown.

reconstructions for the object illuminated by wavelengths of {632.8, 604, and 543 nm} are shown in Figs. 13(d)–13(f) respectively. The corresponding phase images are shown in Figs. 13(g)–13(i).

A pseudocolor multispectral dark-field intensity image is presented in Fig. 14(a) by combining the holograms obtained using red, yellow and green laser illumination. This image demon-

strates that multispectral DIHM reconstruction is possible. To spectrally distinguish cells stained blue requires blue light ( $\lambda < 500$  nm). The tunable HeNe laser used in the experiments presented in this paper<sup>54</sup> did not emit below 543 nm. Using a bright-field Olympus CKX41 microscope with a 10X magnification lens, dark- and bright-field images of MDA-MB-231 cells are presented in Figs. 14(b) and 14(c), respectively. We aim to give the reader a clear comparison between the intensity results from our lensless DIHM presented in this paper and those obtained using a commercial microscope.

The limited spectral range of the tunable laser was overcome, using a tricolor LED. For a number of 10- $\mu$ m-diam latex microspheres. The resulting DIHM bright-field images are presented in Fig. 15. For the reconstruction, the captured intensity hologram, instead of the normalized intensity hologram, was numerically back propagated to the object plane. The sample slide was inserted into a DIHM with  $L = 30$  mm and  $z_0 = 4.6$  mm. The resulting system has magnification  $M = 6.5$  and  $NA = 0.122$ . The lateral resolution of the DIHM with illumination wavelengths of {651, 539, and 474 nm} are  $\delta x = \{2.66, 2.20, \text{ and } 1.94 \mu\text{m}\}$  respectively. This should offer sufficient spatial resolution to image the 10- $\mu$ m-diam microspheres.

The three resulting normalized contrast holograms are presented in Figs. 15(a)–15(c). Intensity reconstructions for the object, illuminated by wavelengths of 651 nm (in the red), 539 nm (in the green), and 474 nm (in the blue), are given in Figs. 15(d)–15(f), respectively, while the corresponding phase images are presented in Figs. 15(g)–15(i). A 100- $\mu$ m-scale bar is inserted into these numerically reconstructed images to aid visualization. One resulting bright-field pseudocolor intensity image of the latex microspheres on a glass slide is presented in Fig. 16. A number of latex microspheres are clearly visible distributed throughout Fig. 16.

To perform cell-viability analysis using the Trypan Blue assay, the ability to spectrally distinguish viable and nonviable cells is fundamentally important. We have presented a simple multispectral DIHM capable of multispectral holographic imaging. Performing the Trypan Blue assay might be possible using the multispectral lensless DIHM presented in this paper.

#### 4.6 Comparisons to a Commercially Available Digital Holographic Microscope

For the slide containing MDA-MB-231 cancer cells, previously examined in Fig. 6, a new image is captured using a DIHM with  $L = 85$  mm,  $z_0 = 17$  mm,  $\lambda = 632.8$  nm,  $NA = 0.0435$ , and having a magnification of  $M = 5$ . The phase-unwrapping algorithm previously examined<sup>63</sup> was applied to the resulting phase information. A three-dimensional representation of the resulting unwrapped phase image is shown in Fig. 17(a). The height profile of the cells calculated from this hologram (see Sec. 4.3) was estimated to be  $\sim 1 \mu\text{m}$ .

A commercially available off-axis DHM was then used to examine the same slide, and the results compared to the results of our lensless DIHM system. The Lyncétec DHM (Ref. 68) employs an off-axis interferometric geometry. Two separate wavefields interfere at small angles to the normal, giving rise to interference fringes. The twin image is thus modulated away from the object image.<sup>2–4</sup> Using a 10x objective lens in the Lyncétec DHM system, an off-axis hologram of the MDA-MB-231 cancer

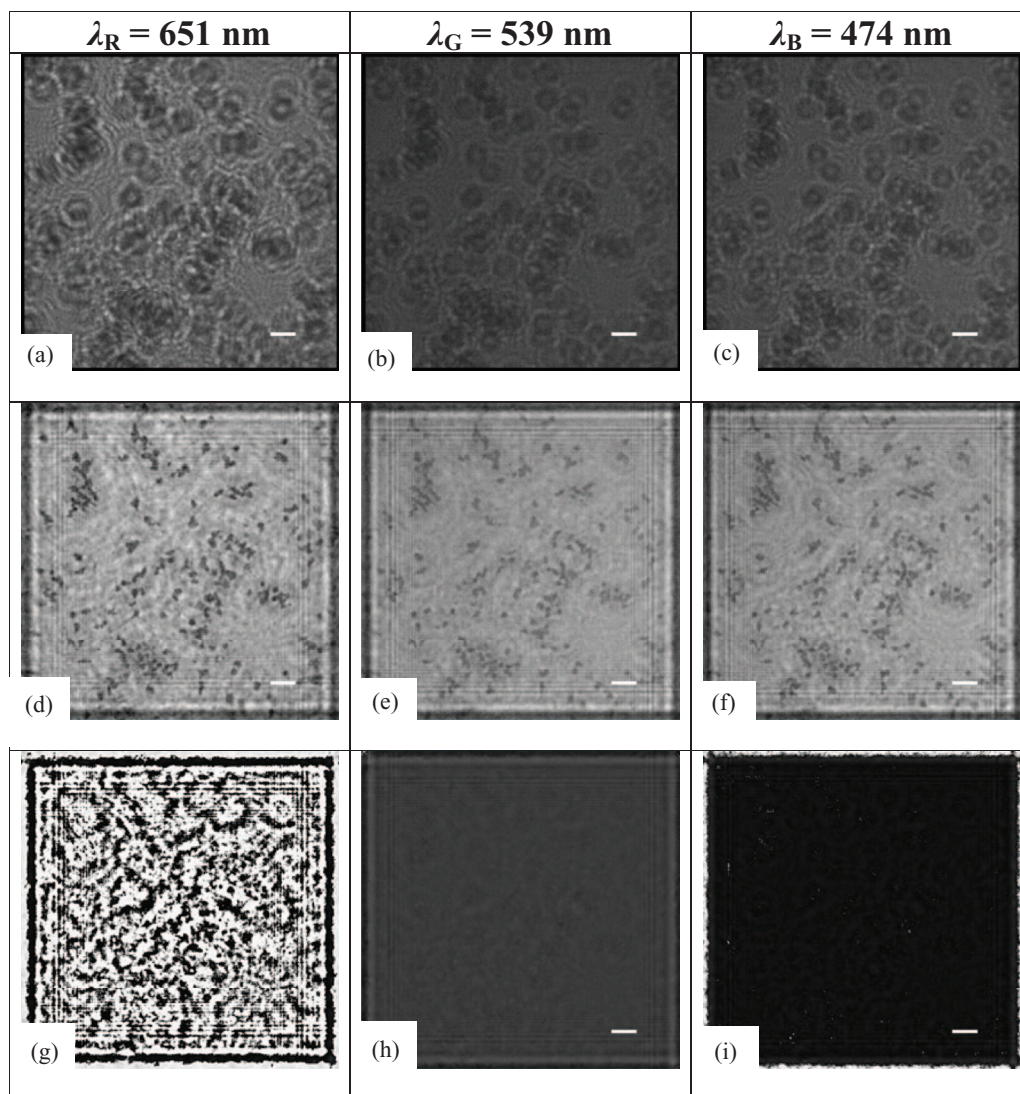


**Fig. 15** Multiple images of the same region of 10- $\mu\text{m}$  latex microspheres using three different LED illuminating wavelengths: 651, 539, and 474 nm. The corresponding holograms, intensity reconstructions, as well as phase images are presented in {(a), (d), and (g)}, {(b), (e), and (h)}, and {(c), (f), and (i)}, respectively. Experimental parameters were  $z_0 = 4.6$  mm,  $L = 30$  mm, magnification = 6.52, and NA = 0.122. A 100- $\mu\text{m}$  bar appears in each reconstructed image.

cells in our sample was captured, processed, and reconstructed. Figure 17(b) shows an unwrapped reconstructed phase image of area 0.16 mm<sup>2</sup>. A visual inspection of the phase results from the commercially available off-axis system [see Fig. 17(b)] reveals typical cell heights in the range  $\pm 682.5$  nm (i.e.,  $\sim 1.365$   $\mu\text{m}$ ). This result is once again  $\approx 1$   $\mu\text{m}$ , obtained using our DIHM to image cells on a 1-mm-thick glass slide.

Therefore, using our lensless DIHM system, implemented with a magnification of 5X, the identification of weakly scattering cells was possible. Furthermore, using a commercially available DHM with a magnification of 10X, similar results were obtained. These results once again support the application of lensless DIHMs as a viable biopharmaceutical microscopic imaging systems.

## 5 Discussion and Conclusions

The aim of this paper was to study the practical use of multispectral lensless DIHMs for biopharmaceutical applications.

The significance of the in-line Gabor DH geometry was, reviewed and various applications, using sources with varying degrees of spatial coherence, were examined. Then the holographic principle was presented with emphasis on microscopic imaging. The problematic twinimage found in DH systems was discussed. It was indicated that the twin image can be neglected because it only appears smeared at the camera due to the geometry of the DIHM. Average image-intensity (DC) suppression was also presented in which the DC term is partially removed to produce the normalized contrast holograms.

An application of the DIHM system was then presented, namely, to detect and count cultured mammalian cells attached to a glass slide substrate. Such cells are of commercial significant because they are grown industrially for large-scale production of biopharmaceuticals.

The principle of operation of the DIHM was introduced in Sec. 2. Lateral and axial resolution limits of the DIHM were considered. The Kirchhoff–Helmholtz transform was reviewed,

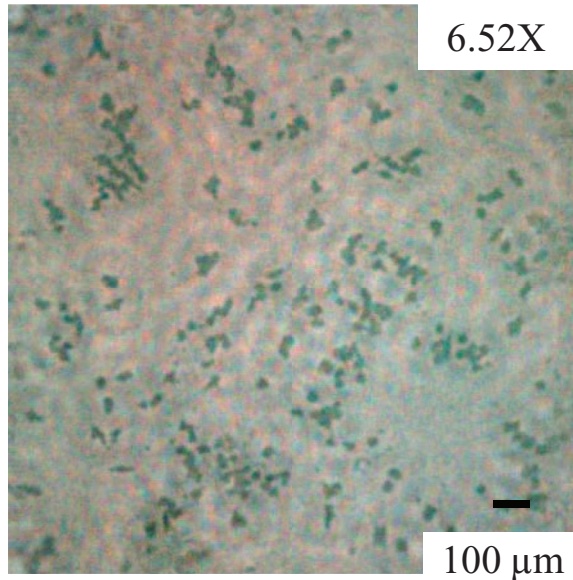


**Fig. 16** Combining the images in Figs. 15(d)–15(f) together to generate a multispectral bright-field image of 10- $\mu\text{m}$  latex microspheres. Experimental parameters were  $z_0 = 4.6$  mm,  $L = 30$  mm, magnification = 6.52, and NA = 0.122. A 100- $\mu\text{m}$  scale bar is included.

and the convolution approach was used to numerically propagate the diffraction field at the camera back to the object plane presented. The experiments performed are then presented in Sec. 3 while the results are discussed in Sec. 4 with several different calibration samples being used.

Single-mode cores of communications optical fibers were successfully imaged using DIHM, using coherent laser illumination. The advantages of DIHM in overcoming the limited depth of focus of conventional compound microscopes was highlighted, and two optical fibers axially displaced  $\sim 1$  mm apart were successfully imaged. However, the limitations of DIHM as a true 3-D imaging technique was illustrated with unsuccessful volume imaging being demonstrated at positions where the fibers overlapped. In this case, the fiber closer to the camera obstructed the view of the fiber placed behind it.

Having demonstrated the imaging capabilities and limitations of DIHM, the percentage confluence of adherent MDA-MB-231 and MCF-7 cells was obtained using light sources of varying spatial coherence (i.e., laser and LED illumination). Percentage confluences of 9.03 and 4.9% were obtained for particular MDA-MB-231 and MCF-7 samples, respectively. Using laser illumination, the extraction of clear phase images of the weakly scattering cells was shown to be possible, while lower intensity LED imaging produced phase images that, following processing, contained considerably more phase discontinuities. This can be attributed to the lower illumination light levels and relatively high SNR arising due to the small aperture of the pinhole used in the LED case to increase the spatial coherence of the secondary source. However, the pinhole diameter of 10  $\mu\text{m}$  ( $\sim 15\lambda$ ) did not result in light as spatially coherent as that emitted by the laser while blocking a great deal of the LED output light. In this paper, we have demonstrated DIHM imaging for biopharmaceutical applications using both laser and LED illumination.

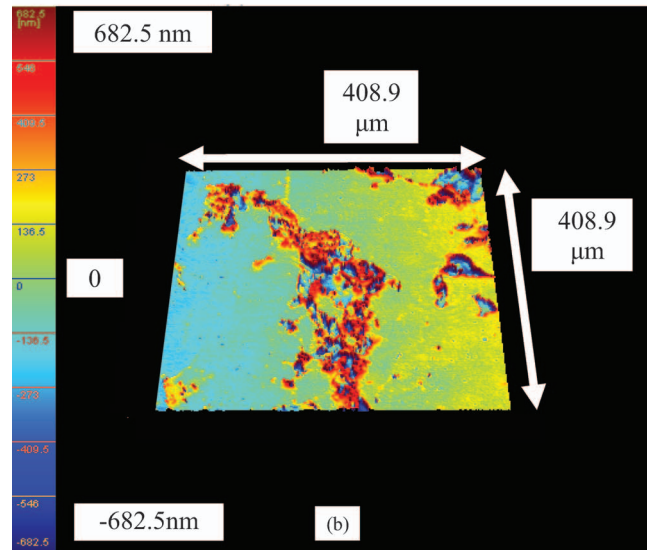
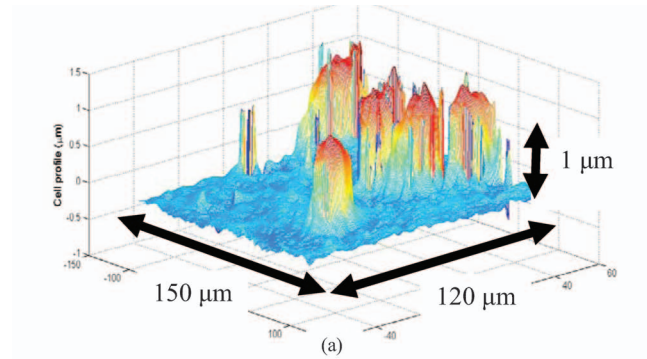


**Fig. 17** (a) The unwrapped phase of the MDA-MB-231 cells using our DIHM system [see Fig. 6(c)]. (b) A sample comparison from the same slide obtained using the commercially available Lyncétec DHM system (Ref. 68). We note that images captured at two different locations on the same slide are presented.

Percentage confluence was discussed, and in order to determine the number of cells present in a sample, areas of interest needed to be identified. A simple filter bank consisting of scaled and rotated versions of a typical cell was created to locate cells of different sizes and orientations. Using this filter bank, 59 MDA-MB-231 cells were detected and counted in the case of laser illumination. On visual inspection of the result, it was found that this very simple system incorrectly identified 4% of cells (false positives) and did not identify a 2% of cells (false negatives).

Having successfully counted cells using the DIHM, multispectral DIHM imaging was then discussed. Using a tunable HeNe laser, dark-field images of MCF-7 cells were obtained. The importance of Trypan Blue assay was reviewed in the context of cell-viability estimation. It was indicated that a bright-field multispectral lensless DIHM using LED illumination could be used for such a purpose. Holograms of latex microspheres with 10- $\mu\text{m}$  diameters were captured and processed using red (651 nm), green (539 nm), and blue (474 nm) LED illumination. Without using a lens, magnifications of up to 6.5X were achieved using the simple multispectral DIHM presented in this paper.

In order to demonstrate that the DIHM can provide a low-cost multispectral holographic imaging system, phase information from a single contrast hologram of weakly scattering MDA-MB-231 cells was captured using the lensless DIHM employing laser illumination. The resulting unwrapped phase image was converted into a height profile. A phase image of the same sample slide was then captured using a commercially available off-axis DHM.<sup>68</sup> The results were comparable, with cellular heights on the order of  $\sim 1 \mu\text{m}$  measured in both cases. Recently, another company announced the production of a commercially available off-axis DHM system.<sup>69</sup>

Although we have reported on an inexpensive multispectral DIHM and demonstrated its capabilities of determining cell counts and percentage confluence for chemically fixed cells, further work is required. To facilitate the off-line Trypan Blue assay analysis, research into the absorption that may complicate holographic imaging will have to be experimentally investigated and verified.

As stated earlier, bioprocesses require constant monitoring. Inline probes exist to perform these measurements.<sup>70</sup> Owing to the limited depth of focus as well as the similar refractive indices of the growth medium and the mammalian cell, cells are not readily distinguishable using systems, such as Mettler/Toledo's particle vision measurement (PVM) particle-analysis system. Access to both the amplitude and phase using holographic imaging may improve functionality of such systems. Indeed, having access to multiple wavelengths especially at nonabsorbed wavelengths, where phase images could quantitatively distinguish cells from the serum-free growth medium or growth medium containing visual pH indicators, such as phenol red.<sup>71</sup>

In summary, a compact multispectral lensless DIHM has been introduced in this paper and implemented using both laser and LED illumination. Multispectral holograms of single-mode communication optical fiber, latex microspheres, and cancer cells were successfully captured and processed. Simple digital processing permitted automated percentage confluence and cell counting. On the basis of the novel results presented here, it is our contention that such a DIHM system could be extended to provide real-time production line analysis in the biopharmaceutical industry subject to specific technological issues as discussed in this paper.

### Acknowledgments

We acknowledge the support of Enterprise Ireland and Science Foundation Ireland under the National Development Plan. We thank Tom O'Reilly and Lynda Hughes for assistance in performing the spectrometer measurement and the cell culture production respectively. We also thank Karen Molony, Nitesh Pandey, and Bryan Hennelly from the National University of Ireland, Maynooth (NUIM), as well as Damien Kelly of Technische Universität, Ilmenau (TU Ilmenau) for helpful discussion and access to the Lyncéetec DHM.

### References

1. D. Gabor, "A new microscopic principle," *Nature* **161**, 777–778 (1948).
2. E. N. Leith and J. Upatnieks, "Reconstructed wavefronts and communication theory," *J. Opt. Soc. Am.* **52**, 1123–1128 (1962).
3. E. N. Leith and J. Upatnieks, "Wavefront reconstruction with continuous-tone objects," *J. Opt. Soc. Am.* **53**, 1377–1381 (1963).
4. E. N. Leith and J. Upatnieks, "Wavefront reconstruction with diffused illumination and three-dimensional objects," *J. Opt. Soc. Am.* **54**, 1295–1301 (1964).
5. J. J. Barton, "Photoelectron holography," *Phys. Rev. Lett.* **61**(12), 1356–1359 (1988).
6. J. J. Barton, "Removing multiple scattering and twin images from holographic images," *Phys. Rev. Lett.* **67**(22), 3106–3109 (1991).
7. J. Sheng, E. Malkiel, and J. Katz, "Digital holographic microscope for measuring three-dimensional particle distributions and motions," *Appl. Opt.* **45**, 3893–3901 (2006).
8. W. Xu, M. H. Jericho, I. A. Meinertzhagan, and H. J. Kreuzer, "Digital in-line holography of microspheres," *Appl. Opt.* **41**, 5367–5375 (2002).
9. L. Repetto, E. Piano, and C. Pontiggia, "Lensless digital holographic microscope with light-emitting diode illumination," *Opt. Lett.* **29**, 1132–1134 (2004).
10. J. P. Ryle, U. Gopinathan, S. McDonnell, T. J. Naughton, and J. T. Sheridan, "Digital in-line holography of biological specimens," *Proc. SPIE* **6311**, 63110C (2006).
11. J. P. Ryle, K. M. Molony, S. McDonnell, T. J. Naughton, and J. T. Sheridan, "Multispectral lensless digital holographic microscope: imaging MCF-7 and MDA-MB-231 cancer cell cultures," *Proc. SPIE* **7442**, 744206 (2009).
12. W. Xu, M. H. Jericho, H. J. Kreuzer, and I. A. Meinertzhagen, "Tracking particles in four dimensions with in-line holographic microscopy," *Opt. Lett.* **28**, 164–166 (2003).
13. L. Repetto, R. Chittofrati, E. Piano, and C. Pontiggia, "Infrared lensless holographic microscope with a vidicon camera for inspection of metallic evaporations on silicon wafers," *Opt. Commun.* **251**, 44–50 (2005).
14. A. Khmaladze, M. Kim, and C.-M. Lo, "Phase imaging of cells by simultaneous dual-wavelength reflection digital holography," *Opt. Express* **16**, 10900–10911 (2008).
15. J. Cheng and S. Han, "On x-ray in-line Gabor holography with a partially coherent source," *Opt. Commun.* **172**, 17–24 (1999).
16. G. Pedrini and H. J. Tiziani, "Short-coherence digital microscopy by use of a lensless holographic imaging system," *Appl. Opt.* **41**, 4489–4496 (2002).
17. U. Gopinathan, G. Pedrini, and W. Osten, "Coherence effects in digital in-line holographic microscopy," *J. Opt. Soc. Am. A* **25**, 2459–2466 (2008).
18. U. Gopinathan, G. Pedrini, B. Javidi, and W. Osten, "Lensless 3D digital holographic microscope imaging at vacuum UV wavelength," *J. Disp. Tech.* **6**, 479–483 (2010).
19. J. W. Goodman and R. W. Lawrence, "Digital image formation from electronically detected holograms," *Appl. Phys. Lett.* **11**, 77–79 (1967).
20. U. Schnars and W. Jüptner, "Direct recording of holograms by a CCD target and numerical reconstruction," *Appl. Opt.* **33**, 179–181 (1994).
21. K. M. Molony, J. P. Ryle, S. McDonnell, J. T. Sheridan, and T. J. Naughton, "Segmentation and visualization of digital in-line holographic microscopy of three-dimensional scenes using reconstructed intensity images," *Proc. SPIE* **7443**, 74431F (2009).
22. J. Garcia-Sucerquia, W. Xu, S. K. Jericho, P. Klages, M. H. Jericho, and H. J. Kreuzer, "Digital in-line holographic microscopy," *Appl. Opt.* **45**, 836–850 (2006).
23. D. P. Kelly, B. M. Hennelly, W. T. Rhodes, and J. T. Sheridan, "Analytical and numerical analysis of linear optical systems," *Opt. Eng.* **45**, 088201 (2006).
24. S. S. Kou and C. J. Sheppard, "Imaging in digital holographic microscopy," *Opt. Express* **15**, 13640–13648 (2007).
25. D. P. Kelly, J. J. Healy, B. M. Hennelly, and J. T. Sheridan, "Quantifying the 2.5D imaging performance of digital holographic systems," *J. Eur. Opt. Soc. Rapid Publications* **6**, 11034 (2011).
26. I. Yamaguchi and T. Zhang, "Phase-shifting digital holography," *Opt. Lett.* **22**, 1268–1270 (1997).
27. J. B. Tiller, A. Barty, D. Paganin, and K. A. Nugent, "The holographic twin image problem: A deterministic phase solution," *Opt. Comm.* **183**, 7–14 (2000).
28. V. Micó, J. García, Z. Zalevsky, and B. Javidi, "Phase-shifting Gabor holography," *Opt. Lett.* **34**, 1492–1494 (2009).
29. Y. Zhang, G. Pedrini, W. Osten, and H. J. Tiziani, "Reconstruction of in-line digital holograms from two intensity measurements," *Opt. Lett.* **29**, 1787–1789 (2004).

30. G. Situ, J. P. Ryle, U. Gopinathan, and J. T. Sheridan, "Generalized in-line digital holographic technique based on intensity measurements at two different planes," *Appl. Opt.* **47**, 711–717 (2008).
31. H. Nyquist, "Certain topics in telegraph transmission theory," *Trans. AIEE* **47**, 617–644 (1928).
32. Kappa DX4 camera, <http://www.iberoptics.com/documentos/DX+4C+-+285+FW.pdf> (August 2010).
33. Hamamatsu C10633 camera, [http://jp.hamamatsu.com/resources/products/sys/pdf/eng/e\\_c10633.pdf](http://jp.hamamatsu.com/resources/products/sys/pdf/eng/e_c10633.pdf) (August 2010).
34. J. J. Healy, B. M. Hennelly, and J. T. Sheridan, "Additional sampling criterion for the linear canonical transform," *Opt. Lett.* **33**, 2599–2601 (2008).
35. Nikon Microscopy education resource, <http://www.microscopyu.com/articles/optics/objectiveproperties.html> (September 2010).
36. F. Zernike, "Phase contrast, a new method for microscopic observation of transparent objects," *Physica* **9**, 686–698 (1942).
37. F. Zernike, "Phase contrast, a new method for microscopic observation of transparent objects: Part II," *Physica* **9**, 686–698 (1942).
38. T. Colomb, N. Pavillon, J. Kühn, E. Cuhe, C. Depeursinge, and Y. Emery, "Extended depth-of-focus by digital holographic microscopy," *Opt. Lett.* **35**, 1840–1842 (2010).
39. T. Wilson and C. J. R. Sheppard, *Theory and Practice of Scanning Optical Microscopy*, Academic Press, London (1984).
40. M. Minsky, "Microscopy Apparatus," U.S. Patent No. 3013467 (December 19, 1961).
41. D. Huang, E. A. Swanson, C. P. Lin, J. S. Schuman, W. G. Stinson, W. Chang, M. R. Hee, T. Flotte, K. Gregory, C. A. Puliafito, and J. G. Fujimoto, "Optical coherence tomography," *Science* **254**, 1178–1181 (1991).
42. J. H. Tjio and T. T. Puck, "Genetics of somatic mammalian cells. II. chromosomal constitution of cells in tissue culture," *J. Exp. Med.* **108**, 259–271 (1958).
43. I. A. MacPherson and M. G. P. Stoker, "Polyoma transformation of hamster cell lines—an investigation of genetic factor affecting cell competence," *Virology* **16**, 147–151 (1962).
44. M. Potter and C. R. Boyce, "Induction of plasma cell neoplasia in strain BALB/c mice with mineral oil and mineral oil adjuvants," *Nature* **193**, 1086–1087 (1962).
45. Wyeth, [www.wyeth.com](http://www.wyeth.com) (July 2009).
46. Genentech, [www.gene.com](http://www.gene.com) (July 2009).
47. Amgen, [www.amgen.com](http://www.amgen.com) (July 2009).
48. H. D. Soule, J. Vazquez, A. Long, S. Albert and M. Brennan, "A human cell line from a pleural effusion derived from a breast carcinoma," *J. Natl. Cancer Inst.* **51**, 1409–1416 (1973).
49. R. Cailleau, R. Young, M. Olive, and W. J. Reeves Jr, "Breast tumor cell lines from pleural effusions," *J. Natl. Cancer Inst.* **53**, 661–674 (1974).
50. M. Wurm, "Production of recombinant protein therapeutics in cultivated mammalian cells," *Nature Biotechnol.* **22**, 1393–1398 (2004).
51. S. Mc Donnell, National Institute for Bioprocessing Research and Training (NIBRT), Private communications (November 2009).
52. Beckman Coulter, [www.beckmancoulter.com](http://www.beckmancoulter.com) (August 2010).
53. S. E. Szabo, "Automating the assessment of cell viability," *Daily Biotech. Updates* **23**, 1–4 (2003).
54. Research Electro-Optics, Inc., multiline HeNe laser, <http://www.reoinc.com/files/FiveLineHeilum.pdf> (August 2010).
55. RGB LED, <http://www2.dealextrême.com/details.dx/sku.20999> (August 2010).
56. J. C. Dainty, *Laser Speckle and Related Phenomena*, Springer, New York 1984.
57. E. Hecht, *Optics*, 4th ed., Addison-Wesley, Reading, MA (2004).
58. J. W. Goodman, *Introduction to Fourier Optics*, 3rd ed., Roberts and Company, Englewood, CO (2004).
59. U. Schnars and W. Jüptner, *Digital Holography*, Springer-Verlag, Berlin (2005).
60. D. P. Kelly, J. T. Sheridan, and W. T. Rhodes, "Fundamental diffraction limitations in a paraxial 4f imaging system with coherent and incoherent illumination," *J. Opt. Soc. Am. A* **24**, 1911–1919 (2007).
61. K. M. Molony, B. M. Hennelly, D. P. Kelly, and T. J. Naughton, "Reconstruction algorithms applied to in-line Gabor digital holographic microscopy," *Opt. Commun.* **283**, 903–909 (2010).
62. D. C. Ghiglia and L. A. Romero, "Robust two-dimensional weighted and unweighted phase unwrapping that uses fast transforms and iterative methods," *J. Opt. Soc. Am. A* **11**, 107–117 (1994).
63. M. A. Schofield and Y. Zhu, "Fast phase unwrapping algorithm for interferometric applications," *Opt. Lett.* **28**, 1194–1197 (2003).
64. K. Murphy, D. Burke, N. Devaney, and C. Dainty, "Experimental detection of optical vortices with a Shack-Hartmann wavefront sensor," *Opt. Express* **18**, 15448–15460 (2010).
65. MCF-cells, <http://www.atcc.org/ATCCAdvancedCatalogSearch/ProductDetails/tabid/452/Default.aspx?ATCCNum=HTB-22&Template=cellBiology> (July 2009).
66. MDA-MB-231 cells, <http://www.atcc.org/ATCCAdvancedCatalogSearch/ProductDetails/tabid/452/Default.aspx?ATCCNum=HTB-26&Template=cellBiology> (July 2009).
67. TIP 112 data sheet, <http://www.datasheetcatalog.org/datasheet/kec/TIP112.pdf> (August 2010).
68. Lyncée Tec, <http://www.lynceetec.com> (August 2010).
69. Phase Holographic Imaging website, <http://www.phiab.se> (September 2010).
70. G. Rudolph, P. Lindner, A. Bluma, K. Joeris, G. Martinez, B. Hitzmann and T. Scheper, "Optical in-line measurement procedures for counting and sizing cells in bioprocess technology," *Adv. Biochem. Eng./Biotechnol.* **116**, 125–142 (2009).
71. R. Ian Freshney, *Culture of Animal Cells A Manual of Basic Technique*, Wiley-Liss, Inc., New York (2000).